Rapid detection and visualization of physiological signatures in cotton leaves under Verticillium wilt stress

Na Wu [a], Pan Gao [b], Jie Wu [a], Yun Zhao [a], Xing Xu [a], Chu Zhang [c], Erik Alexandersson [d], Juan Yang [e], Qinlin Xiao [e,f,*], Yong He [f,*]

[a] School of Artificial Intelligence and Information Engineering, Zhejiang University of Science and Technology, Hangzhou 310023, China
[b] College of Information Science and Technology, Shihezi University, Shihezi 832000, China
[c] School of Information Engineering, Huzhou University, Huzhou 313000, China
[d] Department of Plant Breeding, Swedish University of Agricultural Sciences, P.O. Box 102, 23053 Alnarp, Sweden
[e] Technology Center, China Tobacco Sichuan Industrial Co., Ltd., Chengdu 610066, China
[f] College of Biosystems Engineering and Food Science, Zhejiang University, Hangzhou 310058, China

ARTICLE INFO

ABSTRACT

Verticillium wilt poses a severe threat to cotton growth and significantly impacts cotton yield. It is of significant importance to detect Verticillium wilt stress in time. In this study, the effects of Verticillium wilt stress on the microstructure and physiological indicators (SOD, POD, CAT, MDA, Chl$_a$, Chl$_b$, Chl$_{ab}$, Car) of cotton leaves were investigated, and the feasibility of utilizing hyperspectral imaging to estimate physiological indicators of cotton leaves was explored. The results showed that Verticillium wilt stress-induced alterations in cotton leaf cell morphology, leading to the disruption and decomposition of chloroplasts and mitochondria. In addition, compared to healthy leaves, infected leaves exhibited significantly higher activities of SOD and POD, along with increased MDA amounts, while chlorophyll and carotenoid levels were notably reduced. Furthermore, rapid detection models for cotton physiological indicators were constructed, with the R_p of the optimal models ranging from 0.809 to 0.975. Based on these models, visual distribution maps of the physiological signatures across cotton leaves were created. These results indicated that the physiological phenotype of cotton leaves could be effectively detected by hyperspectral imaging, which could provide a solid theoretical basis for the rapid detection of Verticillium wilt stress.

1. Introduction

Verticillium wilt of cotton (*Gossypium* spp.), caused by the hemibiotrophic fungal pathogen *Verticillium dahliae*, represents a devastating disease in cotton production. The pathogen initially invades the host through the root system, subsequently proliferating and systematically colonizing the plant's vascular tissues. During early infection stages, *Verticillium dahliae* displays biotrophic characteristics, maintaining a relatively asymptomatic phase that minimally affects plant productivity. However, as the infection advances, the pathogen undergoes a critical transition to necrotrophy, actively degrading host tissues to obtain nutrients. This phase manifests as characteristic disease symptoms including vascular wilting, leaf chlorosis, and premature senescence (Zhang et al., 2021a, 2021b). Commonly termed "cotton cancer", Verticillium wilt causes severe physiological disruptions that significantly impair plant growth and development (Ayele et al., 2020). The disease leads to substantial yield losses and marked deterioration of fiber quality. Given the current lack of highly resistant cotton cultivars, early and accurate disease detection becomes paramount for implementing timely and targeted management strategies. Such preventive measures are indispensable for containing disease epidemics and safeguarding cotton production sustainability.

During Verticillium wilt infection, significant alterations in internal tissue structure and physiological parameters occur prior to the manifestation of visible symptoms. When *Verticillium dahliae* invades, the antioxidant system serving as the internal defense mechanism of the host is activated and the activity of related enzymes is stimulated to resist pathogen invasion and maintain normal physiological activities (Kaur et al., 2022). Superoxide dismutase (SOD), peroxidase (POD), catalase (CAT) activities, and malondialdehyde (MDA) amounts are important indicators in the plant antioxidant system (Kaur et al., 2022; Zhu et al.,

* Corresponding authors at: Technology Center, China Tobacco Sichuan Industrial Co., Ltd., Chengdu 610066, China; College of Biosystems Engineering and Food Science, Zhejiang University, Hangzhou 310058, China.
E-mail addresses: qinlxiao@zju.edu.cn (Q. Xiao), yhe@zju.edu.cn (Y. He).

2023). SOD, POD, and CAT can eliminate the harmful oxides in plants, reducing intracellular oxidative stress and damage (Li et al., 2019; Pei et al., 2019). MDA is a byproduct produced by peroxidation between intracellular reactive oxygen species (ROS) and lipids in plants under stress (Ali et al., 2022), and its accumulation is often utilized as an indicator of plant stress levels. In addition, the vascular bundles of cotton are gradually blocked by hyphae and harmful substances as the disease progresses, making normal water transportation difficult (Song et al., 2020; Zhang et al., 2022). Consequently, cotton leaves exhibit progressive wilting initiation, accompanied by interveinal chlorotic lesions that subsequently develop into generalized leaf yellowing and necrosis.

Through monitoring changes in physiological indicators related to the antioxidant system and leaf pigment content, researchers can reveal the interaction mechanism between pathogens and plants and achieve early detection of disease. This has been used for the analysis of plants such as tomatoes, pumpkins, and cotton (Kaur et al., 2024; Khalil et al., 2021; Nafisa Shoaib et al., 2020; Zhang et al., 2021a, 2021b). However, traditional biochemical detection methods for plant physiological signatures often require tedious experimental operations. These methods are invasive to the plants and can only provide data for discrete points, making it impossible to comprehensively investigate time series and distribution of indicators.

In recent years, hyperspectral imaging has been widely used to monitor crop physiological status because of the advantages of integrating image and spectra information obtained from contactless rapid measurement (Sarić et al., 2022). Liu et al. (2021) applied hyperspectral imaging technology to quantify potato nutritional indicators, including petiole nitrate, whole leaf, and vine total nitrate. Asaari et al. (2022) proposed a non-destructive method based on hyperspectral images for the characterization of the effective quantum yield of photosystem II, water potential, transpiration rate, and stomatal conductance of maize under drought stress. Wu et al. (2023a) utilized microscopic hyperspectral imaging technology to dynamically detect CAT activity in tomato leaves. Wang et al. (2021) developed a prediction model for cotton leaf nitrogen concentration by combining the spectral bands sensitive to oxidase activities and leaf nitrogen concentration.

Critical to hyperspectral analysis is the extraction of characteristic wavelengths and the development of robust prediction models. Various feature selection methods, including successive projections algorithm (SPA), random frog (RF), and competitive adaptive reweighted sampling (CARS), have been employed to identify optimal spectral bands while reducing data dimensionality. These selected features are then typically incorporated into machine learning models such as partial least squares regression (PLSR), support vector regression (SVR), and convolutional neural network regression (CNNR) to establish quantitative relationships between spectral signatures and physiological parameters. To the best of our knowledge, however, there are currently few studies linking hyperspectral imaging to efficiently monitor the physiological signatures of cotton under disease stress, especially the various enzyme activities of the antioxidant system. Therefore, this study aimed at dynamic monitoring based on hyperspectral imaging of the physiological phenotype in cotton leaves under Verticillium wilt stress. The specific objectives were: (1) to analyze the effect of Verticillium wilt on the microstructure, physiological signatures, and spectral reflectivity of cotton leaves; (2) to extract characteristic wavelengths correlated with physiological indicators using SPA, RF, and CARS methods and establish accurate prediction models through PLSR, SVR and CNNR approaches; (3) to visualize the spatial distribution of physiological indicators.

2. Materials and methods

2.1. Cotton cultivation and inoculation

Two cultivars of cotton seeds named Xinluzao 45 and Xinluzao 53 (coded as XLZ45 and XLZ53, respectively) were provided by Shihezi

University, China. Normal-sized and undamaged seeds were sown in plastic pots in the greenhouse of the Zijingang Campus of Zhejiang University, China. The greenhouse environment was set to a status with a temperature of 30 °C during the day and 25 °C at night, a photoperiod of 12 h/12 h, and a relative humidity of 60 %. The cultivated soil was a mixture of sandy soil, peat soil, and vermiculite in a ratio of 6:2:1. Normal and consistent water and fertilizer management were carried on all cotton plants.

The *Verticillium dahlia* strain H6 used in this study is a deciduous strain with high pathogenicity and was also provided by Shihezi University. The strain was cultured by incubation on potato glucose agar at 28 °C in darkness until the colonies covered the entire petri dish. The spores were washed from the colonies using sterile water. Then, oscillation and filtering were conducted to obtain a conidia solution. The concentration of the spore suspension was further adjusted to 1×10^7 spores/ml using sterile water.

At the 6–7 true leaves stage, the inoculation was conducted. The cotton plants were carefully removed and the roots were soaked in the spore suspension for 1 h. The plants in the control group were placed in the same volume of sterile water for the same soaking time. After inoculation, the cotton plants were replanted in sterile soil. Cotton in the control and the inoculation groups were cultivated in different pots. The greenhouse temperature was readjusted to 25 °C throughout the day to facilitate the onset of the disease. 360 cotton plants were cultivated, with 180 plants per cultivar. Half (90 plants) were randomly selected from each cultivar for inoculation, and the other half for control.

2.2. Microstructure imaging of cotton leaves

To investigate the effect of Verticillium wilt on the microstructure of cotton leaves, transmission electron microscopy (TEM) was used to image the tissues of healthy and different degrees of infected leaves. The specific sampling location of the infected leaf is shown in Fig. 1.

At the sampling location, the cotton leaves were first sliced to a size of 3×1 mm². The slices were placed in a 2.5 % glutaraldehyde solution and overnight at 4 °C. Then, the slices were rinsed three times with 0.1 M, pH = 7.0 phosphate buffer for 15 min each time. Thereafter, the samples were fixed using 1 % osmium acid solution for 1–2 h in the fume hood and were rinsed using phosphate buffer as before. The samples were dehydrated successively with 30 %, 50 %, 70 %, 80 % ethanol solutions and 90 %, 95 % acetone solutions. The processing time for each concentration of solution was 15 min. The samples were further dehydrated twice with pure acetone for 20 min each time. Finally, the samples were treated with a mixture of Spurr embedding agent and acetone, overnight at room temperature, and then further embedded and heated overnight at 70 °C. The samples were further sliced using the LEICA EM UC7 ultra-thin slicer to obtain slices with a thickness of 70–90 nm. The slices were sequentially dyed in lead citrate solution and uranyl acetate 50 % ethanol saturated solution for 5–10 min. Finally, the Hitachi H-7650 transmission electron microscope was used to observe the microstructure of cotton leaves.

2.3. Hyperspectral image acquisition and spectra extraction

A visible near-infrared hyperspectral imaging system working in line-scanning mode was adopted to obtain hyperspectral images with a spectral range was 414–1017 nm of cotton leaves as described in Bai et al. (2022). Before formal data collection, three system parameters, namely the movement speed of the conveyor belt, the exposure time of the camera, and the distance between the cotton leaves and the camera lens, were repeatedly adjusted for clear and undistorted imaging. These three parameters were finally set to 10 mm/s, 10.5 ms, and 40 cm, respectively. After collecting the hyperspectral images of cotton leaves, black and white board images were also obtained to correct the negative effects of unstable intensity of the light source and instrument dark current on the images in accordance to Bai et al. (2022).

Fig. 1. The sampling locations of healthy and infected cotton leaf tissues.

Hyperspectral images of 322 cotton leaves were collected, including 157 infected leaves (79 for XLZ45 and 78 for XZL53) and 165 healthy leaves (80 for XLZ45 and 85 for XLZ53).

From the corrected hyperspectral images, the band in 778.04 nm with a significant difference in reflectance between the cotton leaves and the background was found using the ENVI (ITT Visual Information Solutions, Boulder, CO, USA) software. Then a simple threshold segmentation combined with morphological operation was performed to obtain the binary mask of cotton leaves. This mask was applied to segment images of other bands, and then the regions of cotton leaves on all band images were obtained. The pixel spectra within these regions in one hyperspectral image were further extracted and preprocessed using wavelet transform with a wavelet basis of Daubechies 5 and a decomposition level of 3 to reduce spectral noise. Finally, the average spectrum of all pixels in one leaf region was calculated to represent the corresponding leaf sample. To facilitate the subsequent modeling analysis, the healthy samples of each cultivar were randomly divided into a training subset and a testing subset at a ratio of 3:1. The same procedure applies to the infected samples. Then the corresponding subsets of healthy and infected samples of both cultivars were merged to constitute the ultimate dataset for predicting corresponding physiological indicators.

2.4. Physiological indicators detection

In this study, the activity of enzymes related to the antioxidant system was determined using the reagent kits from Suzhou Greis Biotechnology Co., Ltd., China. For SOD, the assay kit based on WST-8 method was utilized. WST-8 is a water-soluble tetrazole (WST) salt that can react with O_2- catalyzed by xanthine oxidase, and produces a formazan dye. This reaction can be inhibited by SOD. Thus, the activity of SOD can be indirectly calculated through colorimetric analysis of WST-8 products which have a maximum absorption of light at 450 nm. For POD, the kit is based on its multiple functions of clearing H_2O_2, phenols, and amine toxicity. Under its catalysis, phenolic and amine compounds are oxidized by H_2O_2. The product of this reaction exhibits distinct light absorption at 470 nm. The activity of POD can be determined by measuring the absorbance value at this wavelength. CAT is also a major enzyme scavenging H_2O_2. Under its catalysis, H_2O_2 decomposes to produce water and oxygen. The remaining H_2O_2 in the detection system reacts with 4-Aminoantipyrene which exhibits a characteristic absorption peak at 510 nm. Hence the activity of CAT can be characterized by indirectly calculating the reduction of H_2O_2 per unit time. For MDA, the kit is based on the thiobarbituric acid (TBA) method. MDA can bind with TBA to generate a red complex that exhibits a characteristic absorption peak at 532 nm, through which MDA content can be measured reflecting lipid peroxidation.

In this study, the content of photosynthetic pigments including chlorophyll a, chlorophyll *b*, total chlorophyll, and carotenoids was determined using spectrophotometry. Leaf disc samples with a diameter of 0.86 cm were hole-punched to obtain. The leaf disc samples were then soaked in ethanol with a concentration of 95 % in a dark environment until the leaves turned white. The absorbances of the extract at the wavelengths of 470 nm, 649 nm, and 665 nm were measured using a spectrophotometer (Epoch, BioTek Instruments, Winooski, United States). The concentration of each pigment could be calculated by referring to formulas in the literature (Gao et al., 2022; Song et al., 2021) This operation was repeated three times for each pigment of each sample, and take the average of the measured values as the final representation.

2.5. Characteristic wavelengths extraction

Hyperspectral imaging data exhibit high dimensionality, comprising both physiologically informative features relevant to cotton plant status and substantial spectral redundancy that compromises computational efficiency and model performance. Feature selection methods can select fingerprint wavelengths related to the target task from numerous wavelengths, reducing redundant information and facilitating the establishment of spectral analysis models. This study used SPA, RF, and CARS to screen characteristic wavelengths highly correlated with each physiological indicator. SPA is a forward variable selection algorithm based on variable projection. It can select the wavelength subset with the minimum information redundancy by projecting all wavelengths in vector space (Araújo et al., 2001). RF is an iterative variable selection method. The core idea is to summarize the most useful features by repeatedly randomly selecting some features and evaluating their impact on the results (Li et al., 2012). CARS also selects features through iteration. By combining Monte-Carlo sampling and adaptive reweighting sampling method, the feature set is continuously selected and adjusted to establish the optimal PLSR model (Li et al., 2009).

2.6. Discriminant models construction

To investigate the feasibility of using hyperspectral imaging technology for the rapid detection of physiological indicators of cotton leaves under Verticillium wilt stress, this study introduced traditional PLSR and SVR algorithms and designed a CNNR model according to the characteristics of the dataset. Multiple models were constructed for predicting cotton physiological indicators based on different spectral information.

PLSR is a multiple linear regression method commonly used for spectral analysis. Specifically, it extracts the main characteristic variables of both independent and dependent variables, namely the latent variables, by optimizing their covariance, and establishes the linear

regression model based on the latent variables (Huang et al., 2017). PLSR can effectively avoid the impact of collinearity between variables on model performance and is suitable for scenarios with limited samples. SVR is a support vector machine (SVM) algorithm used for regression tasks, and adept at processing non-linear high-dimensional data. Unlike SVM, the hyperplane searched by SVR should minimize the distance between the sample points farthest from the plane, which helps to minimize the error between the predicted and true values (Awad et al., 2015). For the nonlinear correlations, SVR also needs to employ the kernel function to transform nonlinear variables into a linear space. This study utilized the radial basis function (RBF) as the kernel of SVR. Five-fold cross-validation and a grid-search strategy were utilized for parameter optimization of PLSR and SVR. The search range of the penalty coefficient, c, and the parameter of RBF, g, of SVR were all set to $[10^{-7}, 10^7]$, and the number of the latent variables of PLSR, n_{PLSR}, was set to $[1–30]$.

The structure of the proposed CNNR is shown in Fig. 2. The input spectrum first passed through a Batch Normalization layer for speeding up training by normalizing inputs. Due to the small dataset, we only designed a one-dimensional convolutional layer using ReLU as the activation function to extract key spectral features. The number of convolution kernels was set to 32, and the size and the stride were set to 1×3 and 1, respectively. A max pooling layer with a kernel of 1×2 and a stride of 2 was then connected for feature dimensionality reduction and a batch normalization layer was followed to accelerate model convergence and reduce the risk of overfitting. Finally, two fully connected layers with 64 and 16 neurons were sequentially used to achieve the regression task. The popular L2 Loss was adopted as the loss function of CNNR, while adaptive momentum estimation (Adam) was introduced as the optimization algorithm. During the training process, the initial learning rate of the Adam algorithm was set to 0.01 and decreased by 10 times after every 200 epochs until the loss no longer decreased and remained stable. The batch size was set to 16.

2.7. Visualized analysis

Visualized analysis provides an intuitive channel to better understand the model's performance. In this study, the spectral information
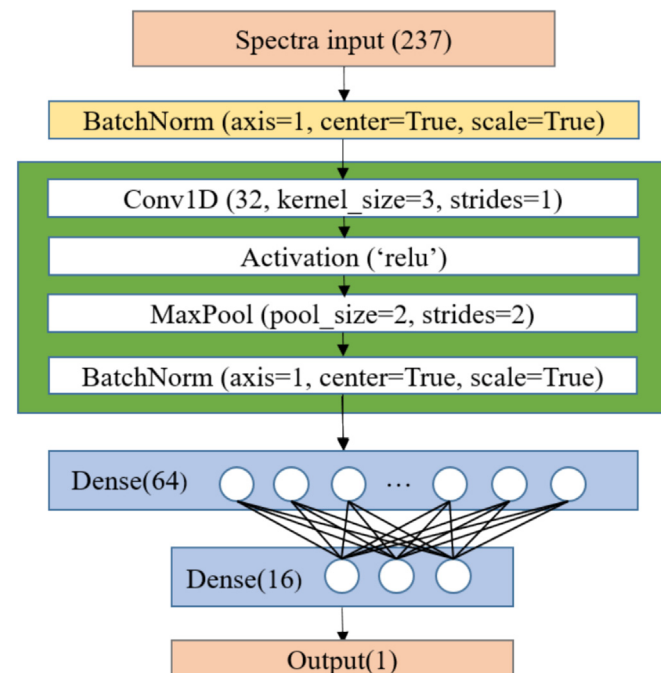

Fig. 2. The architectures of the CNNR model.

of each pixel in the hyperspectral image was used to predict the physiological indicators at the pixel level, and then the visual distribution maps of physiological indicators in cotton leaves were established. The specific steps were as follows. Firstly, the spectral information of each pixel in the hyperspectral image was extracted, and the same spectral preprocessing and wavelength screening operations as in the modeling process were performed. Secondly, the processed pixel spectrum was input into the optimal detection model for each indicator, and obtain the predicted value at the pixel position. Thirdly, referring to the coordinates of each pixel, the predicted value of each indicator was mapped to the hyperspectral image, and different predicted values were displayed in different colors. Ultimately, the visual distribution maps of the activity or content of the physiological indicators in healthy and infected leaves could be drawn.

3. Results and discussion

3.1. Effect of Verticillium wilt on the microstructure of cotton leaves

Using cultivar XLZ53 as a model system, Fig. 3 displays TEM images comparing the ultrastructure of mesophyll cells in healthy cotton leaves and those infected with Verticillium wilt at varying disease severity levels. Healthy leaf samples (Fig. 3 (a)) exhibited intact cellular architecture characterized by: (1) well-defined cell walls, (2) structurally preserved organelles, including spindle-shaped chloroplasts and spherical mitochondria, and (3) limited presence of starch deposits. Progressive disease development induced marked ultrastructural alterations (Fig. 3 (b)–(d)), including (1) cellular deformation, (2) organellar degradation, and (3) significant accumulation of starch granules. These pathological changes, particularly membrane system disruption and organelle damage, represent characteristic stress responses in plants, consistent with previous observations in zinc-stressed maize leaves (Jiang et al., 2007).

Fig. 4 further displays the TEM images of the chloroplasts in the mesophyll cells with different disease severity levels. In healthy mesophyll cells, the chloroplasts possessed a regular arrangement of thylakoids and neatly stacked grana (Fig. 4 (a)). No starch granules were observed in the chloroplast stroma, and the mitochondrial structure was normal. The morphology of chloroplast in the mesophyll cells with mild infection began to change (Fig. 4 (b)). Enlarged starch granules appeared in the chloroplast stroma. The mitochondrial membrane broke down and began to lyse. As the disease progressed, the tissue damage of cotton leaves was aggravated (Fig. 4 (c), (d)). The ratio of the long and short axes of the chloroplasts gradually became imbalanced, resulting in a circular shape. The number of starch granules increased. No clear mitochondria could be observed within the image range.

The appearance and volume enlargement of the starch granules were the defense response of cotton against Verticillium wilt (Khan et al., 2021; Liu et al., 2023). With the deepening of the disease, the chloroplast gradually disintegrated. This also explains the chlorosis of cotton leaves after infection with Verticillium wilt. The chloroplasts are the important sites for photosynthesis and the synthesis of hormones related to defense systems (Hasanuzzaman et al., 2020; Lu and Yao, 2018). Moreover, the chloroplasts also participate in the generation of reactive oxygen species (ROS) and play an important role in the regulation of redox homeostasis in plant cells (Kuźniak and Kopczewski, 2020). The destruction of the chloroplasts in the mesophyll cells reflected that the photosynthesis and self-defense mechanism of cotton were being negatively affected. This will further affect the optical properties of cotton leaves.

3.2. Effects of Verticillium wilt on physiological phenotypic information of cotton leaves

3.2.1. Effects on physiological indicators of antioxidation system

The changes in the measured physiological indicator of the antioxidation system are presented in Table S1. Fig. 5 further summarizes
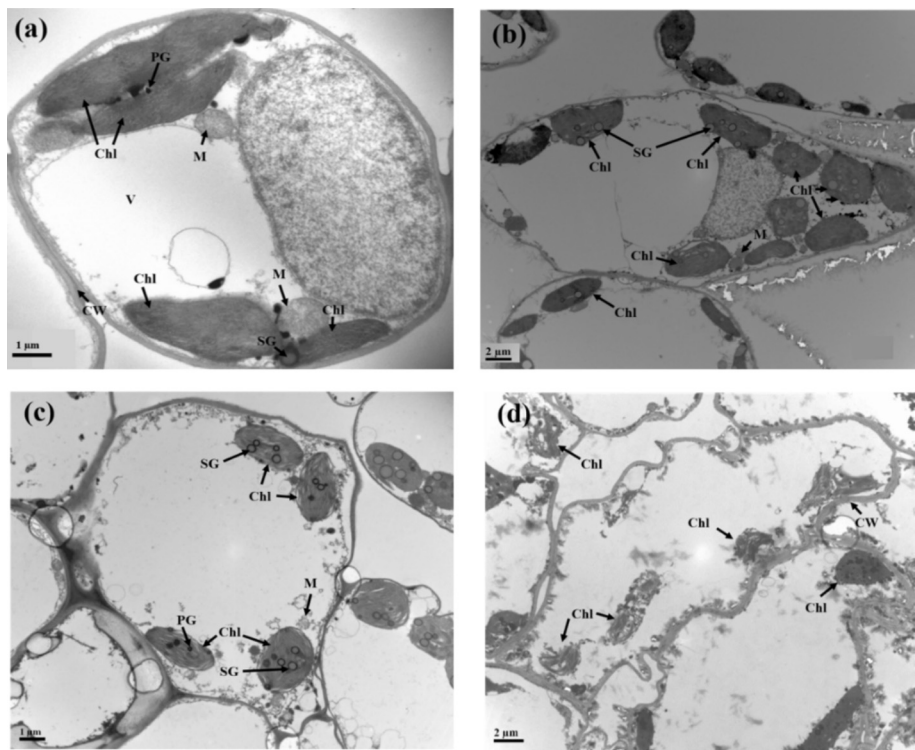
Fig. 3. TEM images of mesophyll cells of healthy (a) and infected (b–d) leaf tissues (M: mitochondria; Chl: chloroplast; PG: plastoglobuli; V: vacuoles; CW: cell wall; SG: starch granule).

means, standard deviations, and significant differences ($p < 0.05$). Both cultivars exhibited significantly higher SOD activity in infected leaves compared to healthy leaves. As a critical enzyme in the plant antioxidant defense system, elevated SOD activity mitigates oxidative damage by scavenging ROS (Mansoor et al., 2022; Sahu et al., 2022). POD activity displayed cultivar-specific responses. While XL45 showed
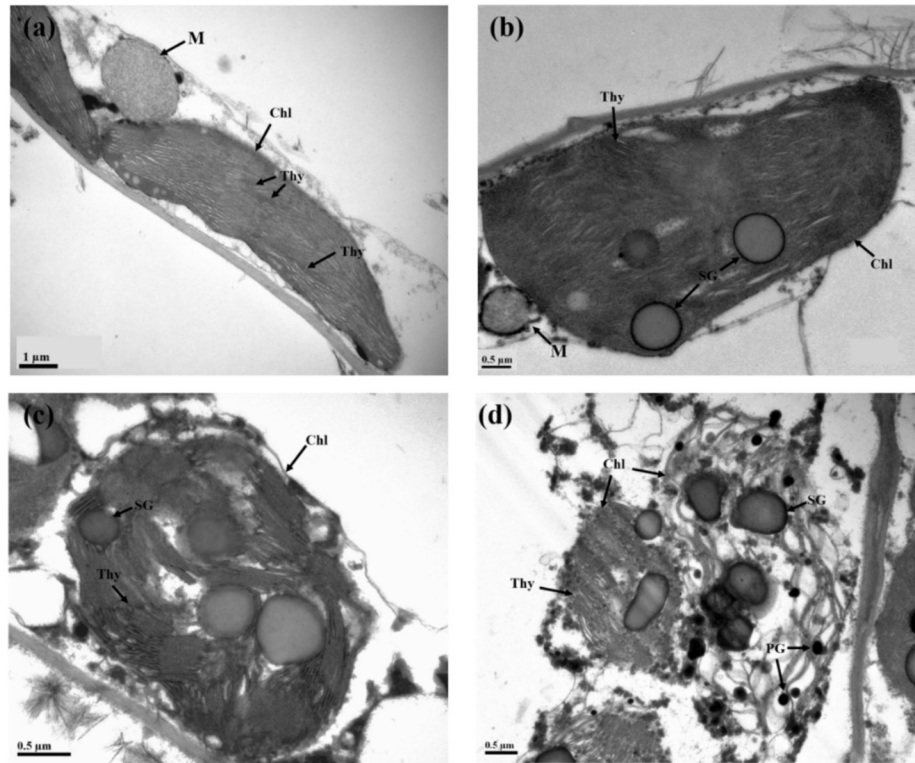

Fig. 4. TEM images of chloroplasts of healthy leaf tissue (a) and infected tissues (b–d) with increasing degree of disease (M: mitochondria; Chl: chloroplast; PG: plastoglobuli; SG: starch granule; Thy: thylakoid).
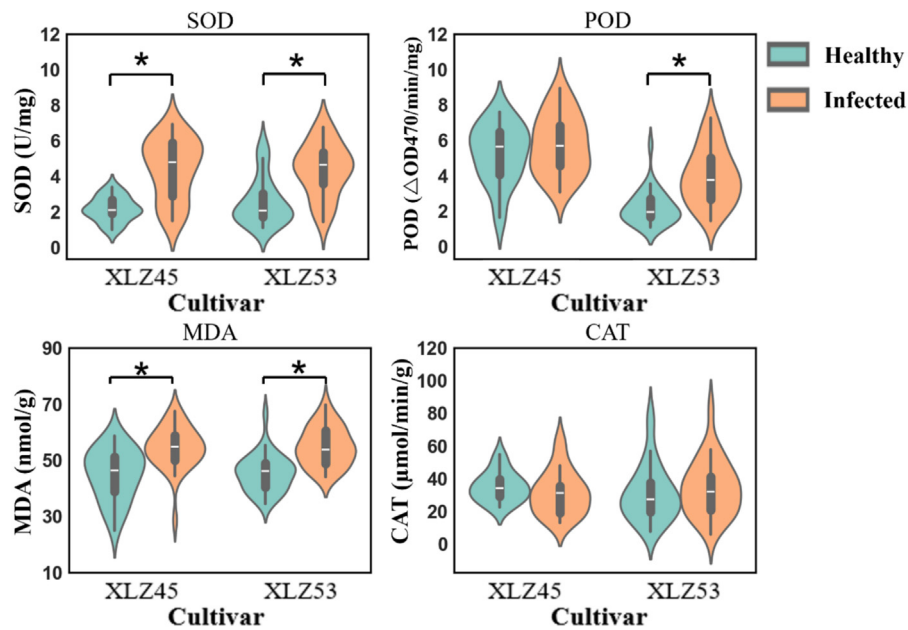
Fig. 5. Effects on the physiological indicators of the antioxidation system of both cultivars (* denotes that there is a significant difference at $p < 0.05$).

no significant difference between infected and healthy leaves, XL53 exhibited a 79.5 % increase in POD activity upon infection ($p < 0.05$). This divergence may reflect intrinsic differences in disease resistance between the two cultivars. Consistent with SOD trends, MDA levels were significantly elevated in infected leaves of both cultivars, indicating Verticillium wilt caused toxic effects of ROS in cotton mesophyll cells, as well as peroxidation of membrane lipids, resulting in membrane damage and increased permeability. This was also consistent with the phenomenon of changes in the microstructure of cotton mesophyll cells under the stress of Verticillium wilt in the previous section. Similar results were also observed in rice under sheath blight stress (Wu et al., 2014) and wheat under low-temperature stress (Liu et al., 2013), reflecting the indicator role of the antioxidant enzyme system in plant stress. No significant differences in CAT activity were detected between healthy and infected leaves in either cultivar. This suggests that the antioxidant response primarily involved SOD and POD upregulation, while CAT played a limited role. The interaction between plants and pathogens involves a series of molecular signaling pathways and biochemical reactions (Kaur et al., 2022; Zhou and Zhang, 2020). Although CAT activity did not show significant differences, the activity of SOD and POD increased to cope with oxidative stress. In this case, the relative inactivity of CAT might not have a significant impact on the overall antioxidant defense. Overall, both cultivars showed activation of their antioxidant defense system in response to oxidative stress after being infected with Verticillium wilt.

3.2.2. Effects on photosynthetic pigments

The statistical information of the photosynthetic pigments of two cultivars is shown in Table S2. Fig. 6 further presents the content distribution of the photosynthetic pigments in healthy and infected leaves of both cultivars. It could be observed that the content of all pigments in the infected leaves of both cultivars was significantly reduced when compared to the healthy leaves, and the relative magnitudes of the reduction were similar, indicating that the effects of Verticillium wilt on the pigment content of the two cultivars were almost identical. Compared to the healthy leaves, the reduced magnitude of pigment content in the infected leaves could be ranked: chlorophyll-a > chlorophyll-b > carotenoids. Chlorophyll-a is the main pigment that captures light energy and converts it into biochemical energy, playing a crucial role

in photosynthesis. Its reduction will hurt the photosynthetic efficiency of plants (Björn et al., 2009). Chlorophyll-b can absorb red and blue light (Naznin et al., 2019). Its reduction might be due to the inhibition of photosynthesis in cotton plants under the stress of Verticillium wilt, which reduced the demand for light energy and thus reduced the synthesis of chlorophyll-b. Carotenoid is an important substance involved in light protection and antioxidant defense. It can help chlorophyll molecules absorb and transfer light energy in photosynthesis, while also neutralizing oxygen free radicals and reducing the damage of oxidative stress to cells (Peñuelas and Munné-Bosch, 2005; Swapnil et al., 2021). In addition, it could be seen from the microstructure of mesophyll cells that disease stress could lead to the destruction of cell structure and the disintegration of chloroplasts (Fig. 3 and 4). The damage to chloroplast structure increased oxidative stress, and the inhibition of photosynthesis caused by Verticillium wilt might all lead to a decrease in the content of photosynthetic pigments. The degree of reduction of different photosynthetic pigments also indirectly reflected their roles and relative importance in this process.

3.3. Spectral characteristic analysis

Fig. 7 presents the average spectral reflectance and standard deviation for healthy and infected leaves of both cultivars. All spectral curves exhibited consistent fluctuation patterns, characteristic of typical green plants (Zhao et al., 2016). Notably, infected leaves of both cultivars showed higher average reflectance than healthy leaves across most wavelengths, with the maximum difference occurring at the 550 nm peak. The spectral differences in the visible region primarily resulted from higher photosynthetic pigment content in healthy leaves, which absorbed more light and consequently exhibited lower reflectance. This observation aligns with established knowledge that 550 nm and 670 nm wavelengths correspond to chlorophyll *a*bsorption peaks (Peñuelas and Filella, 1998). In the near-infrared region, spectral variations were associated with overtone bands of hydrogen-containing groups (C-H, O-H, and N-H) (Ma et al., 2019). These spectral variations might originate from pathophysiological alterations: *Verticillium dahliae* infection in vascular bundles impaired water transport to leaves, with reduced water content potentially increasing near-infrared reflectance; Additionally, the structural damage to mesophyll cells caused by
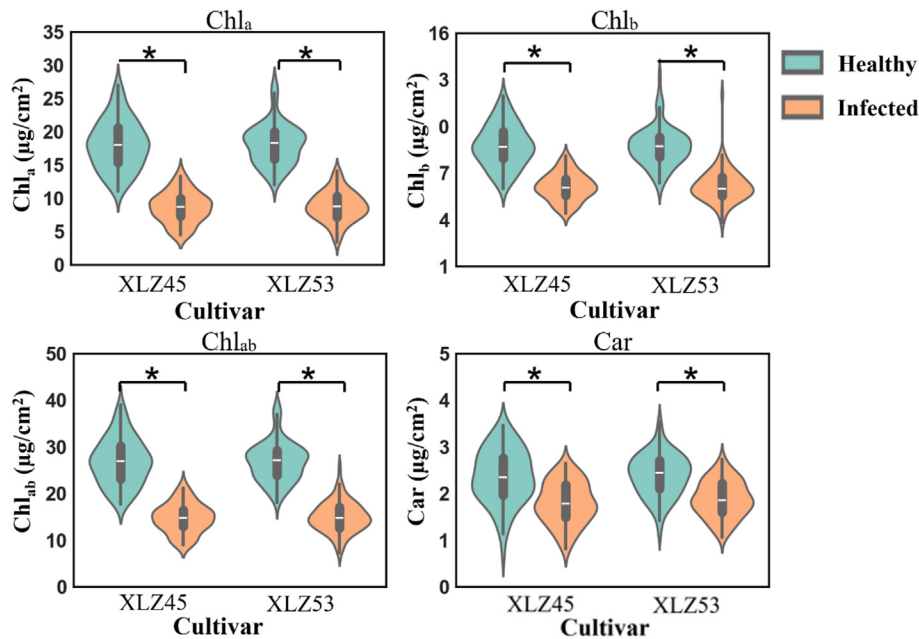
Fig. 6. Effects on the content of photosynthetic pigments of both cultivars (* denotes that there is a significant difference at $p < 0.05$).

bacterial infection affects the scattering and reflection of light, thereby altering the spectral reflectance (Cordon et al., 2022). The red edge transition region (680–750 nm), whose position and shape serve as sensitive indicators of plant health status (Filella and Penuelas, 1994; Shafri and Hamdan, 2009), exhibited a slight blue-shift in infected leaves compared to healthy ones (Fig. 7). This shift reflected the stress condition of the cotton plants.

3.4. Rapid detection of physiological phenotypic information based on full wavelengths

Table 1 exhibited the detection accuracy and precision of physiological indicators of the antioxidation system and photosynthetic pigments using different models based on full wavelengths. For SOD activity, CNNR with an R_p of 0.901 and an *RMSEP* of 0.648 U/mg achieved the best detection results on the testing set. The results of SVR and PLSR were also satisfactory, with R_p greater than 0.8. For POD activity, PLSR performed better than SVR and CNNR, obtaining an R_p of 0.816 and an *RMSEP* of 1.035 △OD470/min/mg, respectively. In terms of CAT activity, CNNR performed the best and got an R_p of 0.801 and an *RMSEP* of 10.264 μmol/min/g, respectively. For MDA content, PLSR stood out from the three models, with the maximal R_p of 0.804 and the

minimum *RMSEP* of 3.221 nmol/g. For Chl_a content, all three models achieved satisfactory results with R_p above 0.95. Among them, SVR performed the best with an R_p of 0.974 and an *RMSEP* of 1.256 μg/cm^2, respectively. In terms of Chl_b and Chl_{ab} content, SVR still performed the best. Specifically, SVR achieved an R_p of 0.941 and an *RMSEP* of 0.584 μg/cm^2 for Chl_b content and obtained an R_p of 0.945 and an *RMSEP* of 2.382 μg/cm^2 for Chl_{ab} content. In terms of Car content, PLSR got the best predictive performance, with a R_p of 0.866, and a *RMSEP* of 0.259 μg/cm^2. On the whole, the detection results of physiological indicators of the antioxidation system and photosynthetic pigments based on full wavelengths were satisfactory.

3.5. Characteristic wavelengths extraction

Fig. 8 displays the characteristic wavelengths selected by SPA, RF, and CARS algorithms, with distinct colors indicating different selection methods. Table S3 provides a comprehensive summary of the specific wavelengths extracted through these approaches. The three methods exhibited varying degrees of dimensionality reduction: SPA retained 4.2–8.5 % of the original spectral features (91.5–95.8 % reduction), RF preserved 6.3 % (93.7 % reduction), while CARS maintained 6.8–23.6 % (76.4–93.2 % reduction). Notably, partial overlap occurred among the
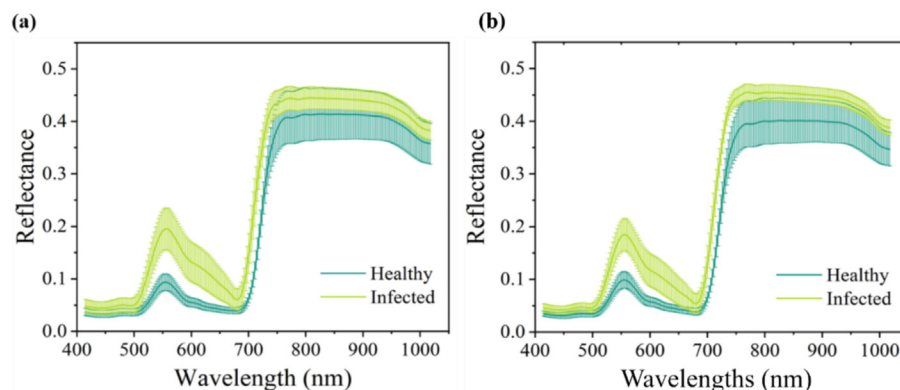

Fig. 7. Average spectra and standard deviations of the healthy and infected leaves of two cultivars (a) XLZ45, (b) XLZ53.

Table 1
The results of models for physiological indicators in cotton leaves using full wavelengths.

Physiological indicator	Model	Parameter	Training set		Testing set	
			R_c	RMSEC	R_p	RMSEP
SOD	PLSR	3	0.936	0.526	0.873	0.729
	SVR	$0.1, 10^3$	0.933	0.538	0.882	0.703
	CNNR	\	0.904	0.640	0.901	0.648
POD	PLSR	10	0.826	1.120	0.816	1.035
	SVR	1.0, 10	0.690	1.439	0.735	1.214
	CNNR	\	0.815	1.152	0.789	1.100
CAT	PLSR	16	0.828	8.050	0.788	10.567
	SVR	$10, 10^2$	0.701	10.237	0.720	11.906
	CNNR	\	0.799	8.615	0.801	10.264
MDA	PLSR	5	0.810	3.578	0.804	3.221
	SVR	0.1, 10	0.740	4.104	0.774	3.433
	CNNR	\	0.838	3.333	0.795	3.288
Chl_a	PLSR	10	0.954	1.678	0.964	1.479
	SVR	$0.1, 10^5$	0.968	1.403	0.974	1.256
	CNNR	\	0.906	1.574	0.970	1.345
Chl_b	PLSR	20	0.906	0.741	0.901	0.746
	SVR	$1.0, 10^2$	0.898	0.768	0.941	0.584
	CNNR	\	0.894	0.780	0.925	0.654
Chl_{ab}	PLSR	4	0.943	2.419	0.933	2.613
	SVR	$0.1, 10^4$	0.960	2.041	0.945	2.382
	CNNR	\	0.953	2.203	0.943	2.417
Car	PLSR	14	0.868	0.259	0.866	0.259
	SVR	$0.1, 10^4$	0.892	0.236	0.854	0.270
	CNNR	\	0.842	0.282	0.791	0.317

Note: In the parameter column, the parameter of PLSR is the number of the latent variables, n_{PLSR}, and the parameters of SVR are the regularization parameter c and the kernel parameter g. The units of RMSEC and RMSEP for SOD are U/mg, for POD are △OD470/min/mg, for CAT are μmol/min/g, for MDA are nmol/g. The units of Chl_a, Chl_b, Chl_{ab}, and Car are all μg/cm^2.

wavelengths selected by different methods, likely attributable to their distinct variable selection mechanisms. The identified characteristic wavelengths showed strong correlations with the physiological indicators investigated in this study. Specifically: the 400–500 nm absorption region corresponded to carotenoid absorption (Zhao et al., 2023); the red-edge region (670–760 nm) demonstrated sensitivity to chlorophyll content and leaf cellular structure (Wu et al., 2023b); the 975–990 nm bands primarily reflected protein-associated N-H stretching second overtone vibrations (Zhao et al., 2014). However, visual assessment alone proved insufficient for evaluating the relative effectiveness of these wavelength selection methods, necessitating further quantitative analysis through predictive modeling.

3.6. Rapid detection of physiological phenotypic information based on characteristic wavelengths

Prediction models for each physiological indicator were developed by combining with different characteristic wavelength selection methods, with results summarized in Tables 2 and 3. For SOD activity prediction, all models based on characteristic wavelengths achieved R_p values exceeding 0.8. The RF-selected wavelengths combined with SVR yielded optimal performance, with an R_p of 0.908 and an RMSEP of 0.624 U/mg, which was superior to the optimal CNNR based on the full wavelengths. Notably, the number of characteristic wavelengths selected by RF was only 6.33 % of the full wavelength set, demonstrating significant practical applicability. For POD activity prediction, model performance ranged from 0.602 to 0.824 in R_p values. PLSR based on the 31 CARS-selected wavelengths showed superior predictive capability, with an R_p of 0.824 and an RMSEP of 1.103 △OD470/min/mg, which outperformed the optimal full-wavelength PLSR model. In terms of CAT activity and MDA content, SVR modeling with 10 SPA-selected wavelengths exhibited the best performance among all tested approaches, achieving the R_p of 0.825 and the RMSEP of 9.680 μmol/min/g for CAT activity and the R_p of 0.809 and the RMSEP of 3.185 nmol/g for MDA content.

For photosynthetic pigment prediction, all three models utilizing characteristic wavelengths demonstrated robust performance. Regarding Chl_a content, The SVR model incorporating SPA-selected wavelengths outperformed all other approaches, including the optimal full-wavelength SVR model. Moreover, the number of characteristic wavelengths selected by SPA was only 6.75 % of the full wavelengths. SPA removed most of the redundant information and facilitated modeling. For Chl_b content, all models achieved excellent performance with R_p exceeding 0.9, and SPA-SVR yielding the best, with the R_p of 0.943 and the RMSEP of 0.573 μg/cm^2. In terms of Chl_{ab} content, the overall performance of SVR was better than that of the PLSR and CNNR. Combined with SPA, SVR achieved the R_p of 0.948 and the RMSEP of 2.323 μg/cm^2. In terms of Car content, most models exhibited satisfactory performance. The SPA-PLSR yielded the best results. The R_p and RMSEP were 0.851 and 0.272 μg/cm^2, respectively, similar to the results of the optimal PLSR model based on the full wavelengths.

The overall detection performance for photosynthetic pigments was superior to that for antioxidant system indicators. This might be attributed to measurement bias stemming from the relative instability of antioxidant indicators, as well as the fact that the spectral range used in detection was primarily associated with pigments. Additionally, most models based on selected characteristic wavelengths achieved similar or better performance compared to those utilizing the full spectral range. Among the wavelength selection methods, models combined with SPA generally outperformed those using RF or CARS in most cases. As illustrated in Fig. 8 and Tables 2–3, SPA selected fewer characteristic wavelengths and eliminated more redundant information, which was likely beneficial for model performance. This finding was consistent with previous studies (Luo et al., 2022; Zhang et al., 2024).

Regarding model selection, SVR was generally superior to PLSR and CNNR. SVR demonstrated strong capabilities in handling both linear and nonlinear problems, whereas CNNR did not exhibit its advantages under the relatively small sample size used in this study. Ng et al. (2020) investigated the impact of training sample size on the performance of deep learning and traditional machine learning models for soil property prediction, recommending a minimum of 2000 samples for effective spectral modeling using deep learning techniques. Similarly, Hong et al. (2022) reported that CNN performed slightly inferior to traditional methods when applied to small datasets.

In summary, by selecting fingerprint spectral wavelengths and eliminating irrelevant or redundant information, the detection models were able to more effectively learn features and predict physiological indicators related to disease. These findings also lay the groundwork for the development of multispectral instruments for future practical field applications.

3.7. Visual distribution of physiological phenotypic information in cotton leaves

For each indicator, the best-performing model mentioned above was selected for constructing the visual distribution map. Fig. 9 illustrates the distribution of antioxidant indicators and photosynthetic pigments in healthy and infected leaves.

For the antioxidant indicators, infected leaves of both cultivars exhibited higher overall SOD and POD activities compared to healthy leaves. Notably, SOD and POD activities were more pronounced near the veins than at the leaf edges in infected leaves. *Verticillium dahliae* invades the xylem vessels through plant roots and produces conidia, which spread upward along the vascular bundle. In response, the plant defense mechanism triggers thin-walled cells to produce biomolecules that, together with mycelial growth, block the ducts. This disrupts water and nutrient transport, ultimately leading to disease development (Zhu et al., 2023). This mechanism likely explained why oxidative stress responses to wilt stress occur earlier near the veins than at the leaf edges. For CAT activity, healthy leaves of XLZ45 showed
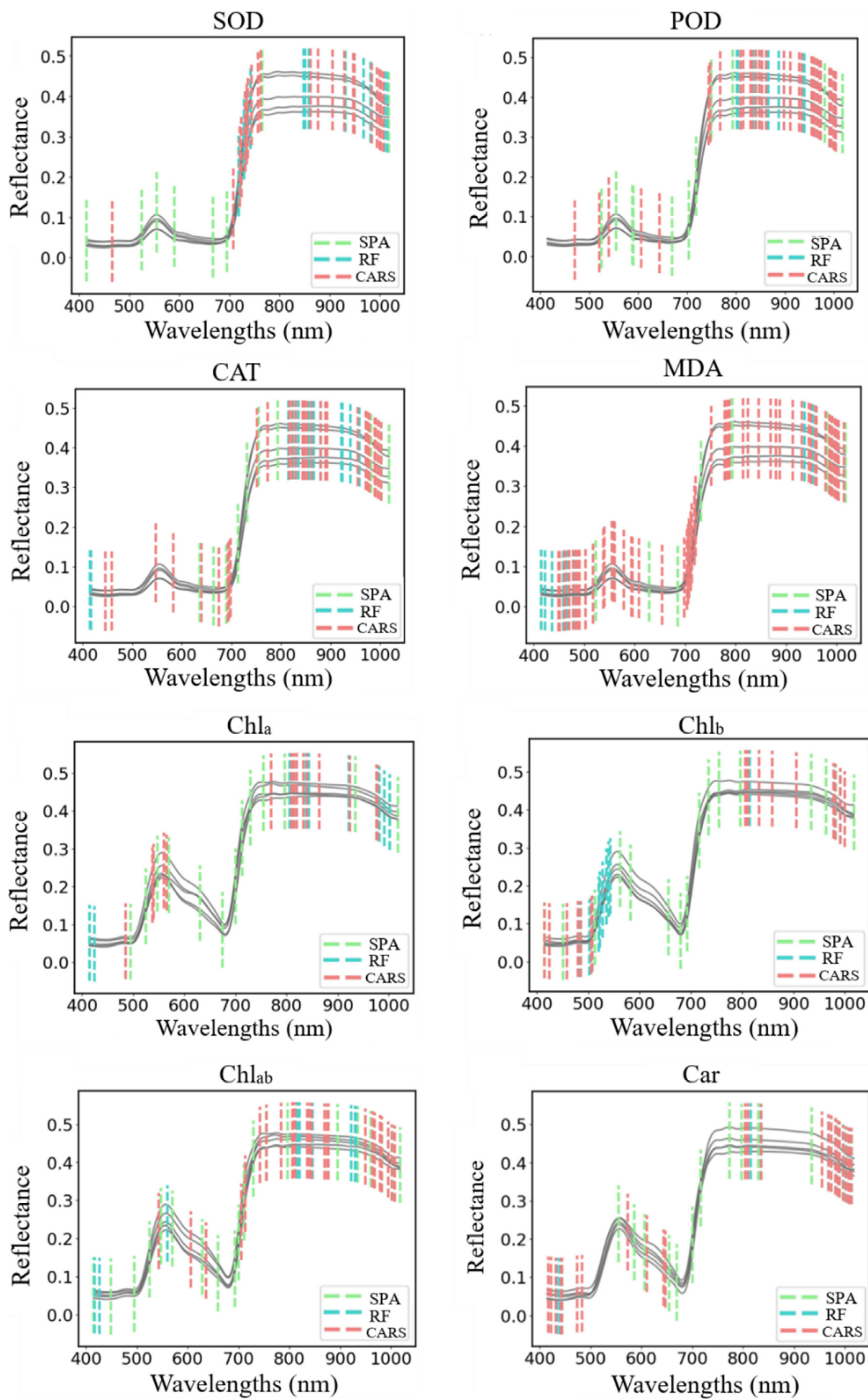
Fig. 8. Characteristic wavelengths selected by SPA, RF, and CARS for different physiological indicators.

Table 2
Results for the indicators of antioxidation system using characteristic wavelengths.

Physiological indicator	Extraction method	Number of wavelengths	Model	Parameter	Training set		Testing set	
					R_c	RMSEC	R_p	RMSEP
			PLSR	5	0.937	0.523	0.869	0.737
	SPA	11	SVR	10, 10^2	0.937	0.525	0.897	0.661
			CNNR	\	0.927	0.560	0.897	0.660
			PLSR	3	0.873	0.732	0.898	0.655
SOD	RF	15	SVR	1, 10^3	0.897	0.633	0.908	0.624
			CNNR	\	0.922	0.580	0.806	0.883
			PLSR	8	0.941	0.505	0.889	0.683
	CARS	21	SVR	1, 10^3	0.930	0.551	0.899	0.652
			CNNR	\	0.927	0.562	0.875	0.721
			PLSR	3	0.783	1.387	0.799	1.076
	SPA	10	SVR	0.1, 10^6	0.767	1.275	0.774	1.133
			CNNR	\	0.787	1.226	0.813	1.042
			PLSR	8	0.811	1.163	0.776	1.128
POD	RF	15	SVR	0.1, 10^6	0.729	1.360	0.625	1.396
			CNNR	\	0.787	1.199	0.602	1.606
			PLSR	9	0.809	1.169	0.824	1.013
	CARS	31	SVR	0.01, 10^6	0.720	1.380	0.764	1.155
			CNNR	\	0.743	1.331	0.751	1.181
			PLSR	5	0.668	10.672	0.742	11.495
	SPA	10	SVR	10, 10^6	0.881	6.786	0.825	9.680
			CNNR	\	0.809	8.423	0.765	11.055
			PLSR	11	0.787	8.848	0.685	12.493
CAT	RF	15	SVR	10, 10^6	0.790	8.797	0.729	11.754
			CNNR	\	0.678	11.061	0.367	14.192
			PLSR	6	0.740	10.119	0.640	11.723
	CARS	31	SVR	10, 10^2	0.697	10.790	0.694	10.989
			CNNR	\	0.792	9.180	0.709	10.751
			PLSR	5	0.813	3.558	0.806	3.208
	SPA	10	SVR	0.01, 10^6	0.812	3.559	0.809	3.185
			CNNR	\	0.826	3.444	0.752	3.576
			PLSR	8	0.825	3.452	0.797	3.276
MDA	RF	15	SVR	0.1, 10^6	0.756	3.993	0.762	3.507
			CNNR	\	0.711	4.290	0.783	3.371
			PLSR	5	0.799	3.669	0.782	3.381
	CARS	56	SVR	0.1, 10^6	0.738	4.122	0.801	3.248
			CNNR	\	0.720	4.236	0.690	3.922

Note: In the parameter column, the parameter of PLSR is the number of the latent variables, n_{PLSR}, and the parameters of SVR are the regularization parameter c and the kernel parameter g. The units of *RMSEC* and *RMSEP* for SOD are U/mg, for POD are △OD470/min/mg, for CAT are μmol/min/g, for MDA are nmol/g.

Table 3
Results for the photosynthetic pigments using characteristic wavelengths.

Physiological indicator	Extraction method	Number of wavelengths	Model	Parameter	Training set		Testing set	
					R_c	RMSEC	R_p	RMSEP
			PLSR	16	0.954	1.677	0.963	1.492
	SPA	16	SVR	10, 10^3	0.969	1.395	0.975	1.230
			CNNR	\	0.961	1.557	0.972	1.307
			PLSR	11	0.948	1.788	0.966	1.443
Chl$_a$	RF	15	SVR	10, 10^6	0.962	1.529	0.944	1.828
			CNNR	\	0.720	3.879	0.744	3.703
			PLSR	10	0.953	1.690	0.960	1.551
	CARS	16	SVR	1, 10^5	0.961	1.549	0.974	1.268
			CNNR	\	0.957	1.635	0.971	1.340
			PLSR	16	0.883	0.819	0.935	0.610
	SPA	17	SVR	10, 10^2	0.898	0.768	0.943	0.573
			CNNR	\	0.899	0.764	0.930	0.636
			PLSR	6	0.856	0.904	0.931	0.630
Chl$_b$	RF	15	SVR	10, 10^4	0.907	0.734	0.941	0.584
			CNNR	\	0.896	0.778	0.922	0.666
			PLSR	9	0.880	0.830	0.922	0.667
	CARS	17	SVR	10, 10^5	0.912	0.719	0.917	0.686
			CNNR	\	0.866	0.873	0.908	0.723
			PLSR	3	0.940	2.476	0.941	2.462
	SPA	20	SVR	10, 10^3	0.964	1.931	0.948	2.323
			CNNR	\	0.960	2.020	0.942	2.450
			PLSR	11	0.949	2.285	0.930	2.670
Chl$_{ab}$	RF	15	SVR	10, 10^5	0.968	1.814	0.941	2.471
			CNNR	\	0.732	4.942	0.653	5.510
	CARS	26	PLSR	4	0.939	2.494	0.941	2.458
			SVR	1, 10^5	0.963	1.963	0.946	2.355

Table 3 (*continued*)

Physiological indicator	Extraction method	Number of wavelengths	Model	Parameter	Training set		Testing set	
					R_c	RMSEC	R_p	RMSEP
			CNNR	\	0.950	2.266	0.929	2.691
			PLSR	12	0.869	0.259	0.851	0.272
	SPA	16	SVR	1, 10^5	0.892	0.237	0.847	0.275
			CNNR	\	0.861	0.265	0.812	0.303
			PLSR	15	0.809	0.307	0.648	0.394
Car	RF	15	SVR	0.1, 10^6	0.765	0.336	0.666	0.387
			CNNR	\	0.701	0.372	0.490	0.452
			PLSR	5	0.819	0.299	0.816	0.300
	CARS	25	SVR	10, 10^2	0.871	0.256	0.849	0.274
			CNNR	\	0.833	0.289	0.813	0.301

Note: In the parameter column, the parameter of PLSR is the number of the latent variables, n_{PLSR}, and the parameters of SVR are the regularization parameter c and the kernel parameter g. The units of Chl_a, Chl_b, Chl_{ab}, and Car are all µg/cm^2.
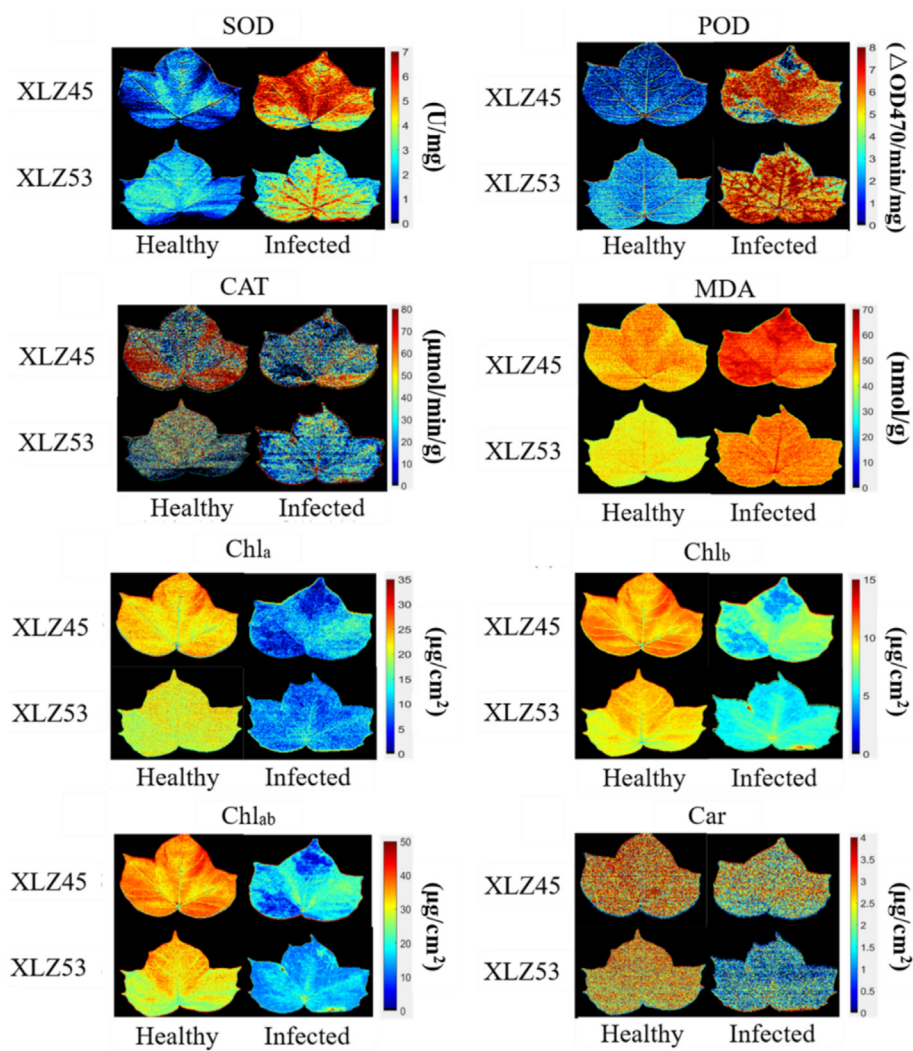

Fig. 9. The visual distribution map developed for antioxidant indicators and photosynthetic pigments.

slightly higher values than infected leaves, whereas the difference between infected and healthy leaves of XLZ53 was minimal—consistent with qualitative analysis results. Both cultivars exhibited higher MDA content in infected leaves compared to healthy leaves, with marginally elevated levels near the veins relative to the edges. The distinct spatial distribution patterns of antioxidant indicators between healthy and infected leaves suggested that ROS homeostasis played a crucial role in cotton's defense against Verticillium wilt, with vein-proximal regions responding earlier to disease stress. Photosynthetic pigment content was significantly higher in healthy leaves of both cultivars than in

infected leaves, confirming that Verticillium wilt stress substantially reduces photosynthetic capacity.

Overall, the visual distribution maps provide intuitive spatial information about disease-related physiological changes in cotton leaves, demonstrating the strong potential of hyperspectral imaging for monitoring plant physiological indicators.

Abbreviations used

Symbols			
SOD	Superoxide dismutase	RF	Random frog
POD	peroxidase	CARS	Competitive adaptive reweighted sampling
CAT	catalase	PLSR	Partial least squares regression
MDA	malondialdehyde	SVR	Support vector regression
Chl_a	Chlorophyll-a	CNNR	Convolutional neural network for regression
Chl_{ab}	Chlorophyll-a and chlorophyll-b	R_c	Correlation coefficient of calibration
Chl_b	Chlorophyll-b	RMSEC	Root mean square error of calibration
Car	Carotenoids	R_p	Correlation coefficient of prediction
SPA	Successive projection algorithm	RMSEP	Root mean square error of prediction

CRediT authorship contribution statement

Na Wu: Writing – review & editing, Writing – original draft, Visualization, Validation, Software, Investigation, Formal analysis, Data curation, Conceptualization. **Pan Gao:** Validation, Methodology, Conceptualization. **Jie Wu:** Validation, Methodology, Conceptualization. **Yun Zhao:** Validation, Methodology, Conceptualization. **Xing Xu:** Writing – review & editing. **Chu Zhang:** Writing – review & editing. **Erik Alexandersson:** Writing – review & editing. **Juan Yang:** Writing – review & editing. **Qinlin Xiao:** Writing – review & editing, Writing – original draft, Visualization, Validation, Software, Investigation, Formal analysis, Data curation, Conceptualization. **Yong He:** Writing – review & editing, Validation, Supervision, Formal analysis, Conceptualization.

Declaration of competing interest

The authors declare that they have no known competing financial interests or personal relationships that could have appeared to influence the work reported in this paper.

Acknowledgments

Appendix A. Supplementary data

Supplementary data to this article can be found online at https://doi.org/10.1016/j.aiia.2025.06.002.

References

Ali, A., Hongbin, L., Rong, L., Zahid, S., Uddin, N., Safir, A., et al., 2022. Physiological and biochemical analysis of ASA-GSH antioxidant system of sea-island cotton in response to verticillium *dahliae*. J. Microbiol. Mol. Genetics 3 (3), 31–55. doi:10.52700/jmmg.v3i3.60.

Araújo, M.C.U., Saldanha, T.C.B., Galvao, R.K.H., Yoneyama, T., Chame, H.C., Visani, V., 2001. The successive projections algorithm for variable selection in spectroscopic multicomponent analysis. Chemom. Intel. Lab. Syst. 57 (2), 65–73. doi:10.1016/S0169-7439(01)00119-8.

Asaari, M.S.M., Mertens, S., Verbraeken, L., Dhondt, S., Inzé, D., Bikram, K., et al., 2022. Nondestructive analysis of plant physiological traits using hyperspectral imaging: A case study on drought stress. Comput. Electron. Agric. 195, 106806. doi:10.1016/j.compag.2022.106806.

Awad, M., Khanna, R., Awad, M., Khanna, R., 2015. Support Vector Regression. Efficient Learning Machines: Theories, Concepts, and Applications for Engineers and System Designers. pp. 67–80.

Ayele, A.G., Wheeler, T.A., Dever, J.K., 2020. Impacts of Verticillium wilt on photosynthesis rate, lint production, and fiber quality of greenhouse-grown cotton (*Gossypium hirsutum*). Plants-Basel 9 (7), 857. doi:10.3390/plants9070857.

Bai, X., Zhou, Y., Feng, X., Tao, M., Zhang, J., Deng, S., et al., 2022. Evaluation of rice bacterial blight severity from lab to field with hyperspectral imaging technique. Front. Plant Sci. 13, 1037774. doi:10.3389/fpls.2022.1037774.

Björn, L.O., Papageorgiou, G.C., Blankenship, R.E., Govindjee., 2009. A viewpoint: why chlorophyll a? Photosynth. Res. 99, 85–98. doi:10.1007/s11120-008-9395-x.

Cordon, G., Andrade, C., Barbara, L., Romero, A.M., 2022. Early detection of tomato bacterial canker by reflectance indices. Inf. Process. Agric. 9 (2), 184–194. doi:10.1016/j.inpa.2021.06.004.

Filella, I., Penuelas, J., 1994. The red edge position and shape as indicators of plant chlorophyll content, biomass and hydric status. Int. J. Remote Sens. 15 (7), 1459–1470. doi:10.1080/01431169408954177.

Gao, Q., Liao, Q., Li, Q., Yang, Q., Wang, F., Li, J., 2022. Effects of LED red and blue light component on growth and photosynthetic characteristics of coriander in plant factory. Horticulturae 8 (12), 1165. doi:10.3390/horticulturae8121165.

Hasanuzzaman, M., Bhuyan, M.B., Parvin, K., Bhuiyan, T.F., Anee, T.I., Nahar, K., et al., 2020. Regulation of ROS metabolism in plants under environmental stress: A review of recent experimental evidence. Int. J. Mol. Sci. 21 (22), 8695. doi:10.3390/ijms21228695.

Hong, S.-J., Yang, T., Kim, S.-Y., Kim, E., Lee, C., Nurhisna, N.I., et al., 2022. Nondestructive prediction of rice seed viability using spectral and spatial information modeling of visible–near infrared hyperspectral images. J. ASABE. 65 (5), 997–1006. doi:10.13031/ja.14982.

Huang, L., Zhou, Y., Meng, L., Wu, D., He, Y., 2017. Comparison of different CCD detectors and chemometrics for predicting total anthocyanin content and antioxidant activity of mulberry fruit using visible and near infrared hyperspectral imaging technique. Food Chem. 224, 1–10. doi:10.1016/j.foodchem.2016.12.037.

Jiang, H., Yang, J., Zhang, J., 2007. Effects of external phosphorus on the cell ultrastructure and the chlorophyll content of maize under cadmium and zinc stress. Environ. Pollut. 147 (3), 750–756. doi:10.1016/j.envpol.2006.09.006.

Kaur, S., Samota, M.K., Choudhary, M., Choudhary, M., Pandey, A.K., Sharma, A., et al., 2022. How do plants defend themselves against pathogens-biochemical mechanisms and genetic interventions. Physiol. Mol. Biol. Pla. 28 (2), 485–504. doi:10.1007/s12298-022-01146-y.

Kaur, T., Mandhania, S., Singh, V., Datten, R., Banakar, P., Malik, K., et al., 2024. Differential biochemical and physiological responses to cotton leaf curl virus infection in contrasting cotton genotypes. Acta Physiol. Plant. 46 (4), 46. doi:10.1007/s11738-024-03678-0.

Khalil, M.I., Youssef, S.A., Tartoura, K.A., Eldesoky, A.A., 2021. Comparative evaluation of physiological and biochemical alteration in tomato plants infected by *Alternaria alternata* in response to *Trichoderma viride* and *Chaetomium globosum* application. Physiol. Mol. Plant Pathol. 115, 101671. doi:10.1016/j.pmpp.2021.101671.

Khan, K.Y., Ali, B., Zhang, S., Stoffella, P.J., Yuan, S., Xia, Q., et al., 2021. Effects of antibiotics stress on growth variables, ultrastructure, and metabolite pattern of *Brassica rapa ssp. chinensis*. Sci. Total Environ. 778, 146333. doi:10.1016/j.scitotenv.2021.146333.

Kuźniak, E., Kopczewski, T., 2020. The chloroplast reactive oxygen species-redox system in plant immunity and disease. Front. Plant Sci. 11, 572686. doi:10.3389/fpls.2020.572686.

Li, H., Liang, Y., Xu, Q., Cao, D., 2009. Key wavelengths screening using competitive adaptive reweighted sampling method for multivariate calibration. Anal. Chim. Acta 648 (1), 77–84. doi:10.1016/j.aca.2009.06.046.

Li, H.D., Xu, Q.S., Liang, Y.Z., 2012. Random frog: an efficient reversible jump markov chain Monte Carlo-like approach for variable selection with applications to gene selection and disease classification. Anal. Chim. Acta 740, 20–26. doi:10.1016/j.aca.2012.06.031.

Li, P.T., Rashid, M.H.O., Chen, T.T., Lu, Q.W., Ge, Q., Gong, W.K., et al., 2019. Transcriptomic and biochemical analysis of upland cotton (*Gossypium hirsutum*) and a chromosome segment substitution line from *G.Hirsutum × G.Barbadense* in response to Verticillium *dahliae* infection. BMC Plant Biol. 19, 1–11. doi:10.1186/s12870-018-1619-4.

Liu, N., Townsend, P.A., Naber, M.R., Bethke, P.C., Hills, W.B., Wang, Y., 2021. Hyperspectral imagery to monitor crop nutrient status within and across growing seasons. Remote Sens. Environ. 255, 112303. doi:10.1016/j.rse.2021.112303.

Liu, W., Yu, K., He, T., Li, F., Zhang, D., Liu, J., 2013. The low temperature induced physiological responses of *Avena nuda L.*, a cold-tolerant plant species. Scientific World J. 2013 (1), 658793. doi:10.1155/2013/658793.

Liu, Z., Wu, X., Hou, L., Ji, S., Zhang, Y., Fan, W., et al., 2023. Effects of cadmium on transcription, physiology, and ultrastructure of two tobacco cultivars. Sci. Total Environ. 869, 161751. doi:10.1016/j.scitotenv.2023.161751.

Lu, Y., Yao, J., 2018. Chloroplasts at the crossroad of photosynthesis, pathogen infection and plant defense. Int. J. Mol. Sci. Int. J. Mol. Sci. 19 (12), 3900. doi:10.3390/ijms19123900.

Luo, W., Tian, P., Fan, G., Dong, W., Zhang, H., Liu, X., 2022. Non-destructive determination of four tea polyphenols in fresh tea using visible and near-infrared spectroscopy. Infrared Phys. Techn. 123, 104037. doi:10.1016/j.infrared.2022.104037.

Ma, L., Peng, Y., Pei, Y., Zeng, J., Shen, H., Cao, J., et al., 2019. Systematic discovery about NIR spectral assignment from chemical structural property to natural chemical compounds. Sci. Rep. 9 (1), 9503. doi:10.1038/s41598-019-45945-y.

Mansoor, S., Ali Wani, O., Lone, J.K., Manhas, S., Kour, N., Alam, P., et al., 2022. Reactive oxygen species in plants: from source to sink. Antioxidants 11 (2), 225. doi:10.3390/antiox11020225.

Nafisa Shoaib, A., Iqbal, J., Khan, K.A., 2020. Evaluation of phenotypic, physiological and biochemical attributes connected with resistance in tomato against *Alternaria solani*. Acta Physiol. Plant. 42, 1–17. doi:10.1007/s11738-020-03076-2.

Naznin, M.T., Lefsrud, M., Gravel, V., Azad, M.O.K., 2019. Blue light added with red LEDs enhance growth characteristics, pigments content, and antioxidant capacity in lettuce, spinach, kale, basil, and sweet pepper in a controlled environment. Plants 8 (4), 93. doi:10.3390/plants8040093.

Ng, W., Minasny, B., Mendes, W.d.S., Demattê, J.A.M., 2020. The influence of training sample size on the accuracy of deep learning models for the prediction of soil properties with near-infrared spectroscopy data. Soil 6 (2), 565–578. doi:10.5194/soil-6-565-2020.

Pei, Y., Li, X., Zhu, Y., Ge, X., Sun, Y., Liu, N., et al., 2019. GhABP19, a novel germin-like protein from *Gossypium hirsutum*, plays an important role in the regulation of resistance to Verticillium and fusarium wilt pathogens. Front. Plant Sci. 10. doi:10.3389/fpls.2019.00583.

Peñuelas, J., Filella, I., 1998. Visible and near-infrared reflectance techniques for diagnosing plant physiological status. Trends Plant Sci. 3 (4), 151–156. doi:10.1016/S1360-1385(98)01213-8.

Peñuelas, J., Munné-Bosch, S., 2005. Isoprenoids: an evolutionary pool for photoprotection. Trends Plant Sci. 10 (4), 166–169. doi:10.1016/j.tplants.2005.02.005.

Sahu, P.K., Jayalakshmi, K., Tilgam, J., Gupta, A., Nagaraju, Y., Kumar, A., et al., 2022. ROS generated from biotic stress: effects on plants and alleviation by endophytic microbes. Front. Plant Sci. 13, 1042936. doi:10.3389/fpls.2022.1042936.

Sarić, R., Nguyen, V.D., Burge, T., Berkowitz, O., Trtílek, M., Whelan, J., et al., 2022. Applications of hyperspectral imaging in plant phenotyping. Trends Plant Sci. 27 (3), 301–315. doi:10.1016/j.tplants.2021.12.003.

Shafri, H.Z., Hamdan, N., 2009. Hyperspectral imagery for mapping disease infection in oil palm plantation using vegetation indices and red edge techniques. Am. J. Appl. Sci. 6 (6), 1031–1035.

Song, D., Gao, D., Sun, H., Qiao, L., Zhao, R., Tang, W., et al., 2021. Chlorophyll content estimation based on cascade spectral optimizations of interval and wavelength characteristics. Comput. Electron. Agric. 189, 106413. doi:10.1016/j.compag.2021.106413.

Song, R., Li, J., Xie, C., Jian, W., Yang, X., 2020. An overview of the molecular genetics of plant resistance to the Verticillium wilt pathogen Verticillium *dahliae*. Int. J. Mol. Sci. 21 (3), 1120. doi:10.3390/ijms21031120.

Swapnil, P., Meena, M., Singh, S.K., Dhuldhaj, U.P., Marwal, A., 2021. Vital roles of carotenoids in plants and humans to deteriorate stress with its structure, biosynthesis, metabolic engineering and functional aspects. Curr. Plant Biol. 26, 100203. doi:10.1016/j.cpb.2021.100203.

Wang, J., Tian, T., Wang, H., Cui, J., Zhu, Y., Zhang, W., et al., 2021. Estimating cotton leaf nitrogen by combining the bands sensitive to nitrogen concentration and oxidase activities using hyperspectral imaging. Comput Electron Agric. 189, 106390. doi:10.1016/j.compag.2021.106390.

Wu, G., Fang, Y., Jiang, Q., Cui, M., Li, N., Ou, Y., et al., 2023b. Early identification of strawberry leaves disease utilizing hyperspectral imaging combing with spectral features, multiple vegetation indices and textural features. Comput. Electron. Agric. 204, 107553. doi:10.1016/j.compag.2022.107553.

Wu, L., Zhang, Y., Jiang, Q., Zhang, Y., Ma, L., Ma, S., et al., 2023a. Study on CAT activity of tomato leaf cells under salt stress based on microhyperspectral imaging and transfer learning algorithm. Spectrochim. Acta A 302, 123047. doi:10.1016/j.saa.2023.123047.

Wu, W., Wan, X., Shah, F., Fahad, S., Huang, J., 2014. The role of antioxidant enzymes in adaptive responses to sheath blight infestation under different fertilization rates and hill densities. Scientific World J. 2014 (1), 502134. doi:10.1155/2014/502134.

Zhang, D.D., Dai, X.F., Klosterman, S.J., Subbarao, K.V., Chen, J.Y., 2022. The secretome of Verticillium *dahliae* in collusion with plant defence responses modulates Verticillium wilt symptoms. Biol. Rev. 97 (5), 1810–1822. doi:10.1111/brv.12863.

Zhang, S., Liu, J., Xu, B., Zhou, J., 2021b. Differential responses of Cucurbita pepo to *Podosphaera xanthii* reveal the mechanism of powdery mildew disease resistance in pumpkin. Front. Plant Sci. 12, 633221. doi:10.3389/fpls.2021.633221.

Zhang, T., Lu, L., Song, Y., Yang, M., Li, J., Yuan, J., et al., 2024. Non-destructive identification of *Pseudostellaria heterophylla* from different geographical origins by Vis/NIR and SWIR hyperspectral imaging techniques. Front. Plant Sci. 14, 1342970. doi:10.3389/fpls.2023.1342970.

Zhang, Y., Gao, Y., Wang, H.L., Kan, C., Li, Z., Yang, X., et al., 2021a. Verticillium *dahlia* secretory effector PevD1 induces leaf senescence by promoting ORE1-mediated ethylene biosynthesis. Mol. Plant 14 (11), 1901–1917.

Zhao, H., Guo, B., Wei, Y., Zhang, B., 2014. Effects of grown origin, genotype, harvest year, and their interactions of wheat kernels on near infrared spectral fingerprints for geographical traceability. Food Chem. 152, 316–322. doi:10.1016/j.foodchem.2013.11.122.

Zhao, J., Chen, N., Zhu, T., Zhao, X., Yuan, M., Wang, Z., et al., 2023. Simultaneous quantification and visualization of photosynthetic pigments in *Lycopersicon esculentum mill*. Under different levels of nitrogen application with visible-near infrared hyperspectral imaging technology. Plants 12 (16), 2956. doi:10.3390/plants12162956.

Zhao, Y.R., Li, X., Yu, K.Q., Cheng, F., He, Y., 2016. Hyperspectral imaging for determining pigment contents in cucumber leaves in response to angular leaf spot disease. Sci. Rep. 6 (1), 27790. doi:10.1038/srep27790.

Zhou, J.M., Zhang, Y., 2020. Plant immunity: danger perception and signaling. Cell 181 (5), 978–989. doi:10.1016/j.cell.2020.04.028.

Zhu, Y., Zhao, M., Li, T., Wang, L., Liao, C., Liu, D., et al., 2023. Interactions between Verticillium *dahliae* and cotton: pathogenic mechanism and cotton resistance mechanism to Verticillium wilt. Front. Plant Sci. 14, 1174281. doi:10.3389/fpls.2023.1174281.